Science Advances
AAAS

Supplementary Materials for

Single-shot deterministic complex amplitude imaging with a single-layer metalens

Liu Li *et al.*

Corresponding author: Yuanmu Yang, ymyang@tsinghua.edu.cn

Sci. Adv. **10**, eadl0501 (2024)
DOI: 10.1126/sciadv.adl0501

The PDF file includes:

Other Supplementary Material for this manuscript includes the following:

Supplementary Text

Text S1. Working principle of the metalens-assisted single-shot complex amplitude imaging system

In the proposed metalens-assisted complex amplitude imaging system, for a linearly polarized incident light whose polarization direction is at an angle Φ with respect to the x-axis, the light field can be decomposed into two replicated left- and right-handed circularly polarized (LCP and RCP) light field U_{LCP} and U_{RCP} with a shearing distance Δs in the x- or y-direction, which can be written as,

$$U_{\mathrm{LCP}}=\frac{\sqrt{2}}{2}\begin{bmatrix}1\\ i\end{bmatrix}A_{\mathrm{LCP}}\exp[i\varphi(x,y)], \tag{S1}$$

$$U_{\mathrm{RCP}}=\frac{\sqrt{2}}{2}\begin{bmatrix}1\\ -i\end{bmatrix}A_{\mathrm{RCP}}\exp[i\varphi(x,y)]\exp\left[i\nabla_{x/y}\varphi\times\Delta s\right]\exp[-i2\Phi], \tag{S2}$$

where A_{LCP} and A_{RCP} are the amplitude of the LCP and RCP light field, respectively, $\varphi(x, y)$ is the phase distribution, and $\nabla_{x/y}\varphi$ is the phase gradient along the x- or y-direction. The shearing interference pattern is then captured by the polarization camera. By applying the Jones matrix of the four linear micro-polarizers (0°, 45°, 90°, and 135°) at each macro-pixel of the polarization camera, the shearing interference light intensity captured by the polarization camera can be calculated as,

$$I_{0^\circ}=\left|\begin{bmatrix}1 & 0\\ 0 & 0\end{bmatrix}(U_{\mathrm{LCP}}+U_{\mathrm{RCP}})\right|^2=I_{\mathrm{LCP}}+I_{\mathrm{RCP}}+2\sqrt{I_{\mathrm{LCP}}I_{\mathrm{RCP}}}\cos(\theta-2\Phi), \tag{S3}$$

$$I_{45^\circ}=\left|\frac{1}{2}\begin{bmatrix}\sqrt{2} & \sqrt{2}\\ 0 & 0\end{bmatrix}(U_{\mathrm{LCP}}+U_{\mathrm{RCP}})\right|^2=I_{\mathrm{LCP}}+I_{\mathrm{RCP}}+2\sqrt{I_{\mathrm{LCP}}I_{\mathrm{RCP}}}\cos\left(\theta-\frac{\pi}{2}-2\Phi\right), \tag{S4}$$

$$I_{90^\circ}=\left|\begin{bmatrix}0 & 0\\ 0 & 1\end{bmatrix}(U_{\mathrm{LCP}}+U_{\mathrm{RCP}})\right|^2=I_{\mathrm{LCP}}+I_{\mathrm{RCP}}+2\sqrt{I_{\mathrm{LCP}}I_{\mathrm{RCP}}}\cos(\theta+\pi-2\Phi), \tag{S5}$$

$$I_{135^\circ}=\left|\frac{1}{2}\begin{bmatrix}\sqrt{2} & -\sqrt{2}\\ 0 & 0\end{bmatrix}(U_{\mathrm{LCP}}+U_{\mathrm{RCP}})\right|^2=I_{\mathrm{LCP}}+I_{\mathrm{RCP}}+2\sqrt{I_{\mathrm{LCP}}I_{\mathrm{RCP}}}\cos\left(\theta+\frac{\pi}{2}-2\Phi\right), \tag{S6}$$

where $I=|U_{\mathrm{LCP/RCP}}|^2$ is the light intensity and $\theta=\nabla_{x/y}\varphi\times\Delta s$. Combining Eqs. (S3)-(S6), the phase gradients along the x-direction or y-direction can be calculated as,

$$\nabla_{x/y}\varphi=\frac{1}{\Delta s}\operatorname{atan}\left(\frac{I_{0^\circ}-I_{90^\circ}}{I_{45^\circ}-I_{135^\circ}}\right)+\frac{2\Phi}{\Delta s}. \tag{S7}$$

Note that $2\Phi/\Delta s$ is a constant term and can be removed by the calibration process (see text S3 for more details). Therefore, the polarization orientation of the incident light can be set to any arbitrary direction.

To simultaneously obtain phase gradients $\nabla_x\varphi$ and $\nabla_y\varphi$ in a captured image, as shown in Fig. 1 of the main text, our approach is to use the metalens to generate a spatially-multiplexed point spread functions (PSFs). Afterward, the phase distribution can be reconstructed using the higher-order finite-difference-based least-squares integration (HFLI) method (see Supplementary Information Section 2 for details).

The light intensity can be calculated from the sum of the light intensities of two arbitrary orthogonal linear polarizations as,

$$I_{\mathrm{total}}=I_{0^\circ}+I_{90^\circ}=I_{45^\circ}+I_{135^\circ}. \tag{S8}$$

Text S2. Algorithm for phase reconstruction from the phase gradients

To reconstruct the 2D phase distribution from phase gradients along both directions, here we use the higher-order finite-difference-based least-squares integration (HFLI) method (46). The

HFLI method is widely used for wavefront reconstruction due to the relatively fast reconstruction speed. The phase gradients are represented pixel-wise as,

$$S_{\mathrm{x}} = \left[\frac{\partial\varphi(x_1, y_1)}{\partial x}; \frac{\partial\varphi(x_1, y_2)}{\partial x}; \ldots; \frac{\partial\varphi\left(x_{\mathrm{k}}, y_{\mathrm{j}}\right)}{\partial x}; \ldots; \frac{\partial\varphi(x_{\mathrm{K}}, y_{\mathrm{J}})}{\partial x}\right],$$

$$S_{\mathrm{y}} = \left[\frac{\partial\varphi(x_1, y_1)}{\partial y}; \frac{\partial\varphi(x_1, y_2)}{\partial y}; \ldots; \frac{\partial\varphi\left(x_{\mathrm{k}}, y_{\mathrm{j}}\right)}{\partial y}; \ldots; \frac{\partial\varphi(x_{\mathrm{K}}, y_{\mathrm{J}})}{\partial y}\right], \tag{S9}$$

where x_{k} and y_{j} are the coordinates of each macro-pixel in the polarization camera, K and J are the number of sampling points along the x- and y- direction, respectively. In the Southwell configuration, the relationship between the local wavefront and the phase gradient can be expressed as,

$$\frac{\varphi_{\mathrm{k,j+1}} - \varphi_{\mathrm{k,j}}}{L} = \frac{s^{\mathrm{x}}_{\mathrm{k,j+1}} + s^{\mathrm{x}}_{\mathrm{k,j}}}{2}, \ (k = 1, 2, \ldots, \mathrm{K}; j = 1, 2, \ldots, J\text{-}1), \tag{S10}$$

$$\frac{\varphi_{\mathrm{k,j+1}} - \varphi_{\mathrm{i,j}}}{L} = \frac{s^{\mathrm{y}}_{\mathrm{k+1,j}} + s^{\mathrm{y}}_{\mathrm{i,j}}}{2}, \ (k = 1, 2, \ldots, \mathrm{K}\text{-}1; j = 1, 2, \ldots, J), \tag{S11}$$

where L = 6.9 μm is the macro-pixel size. $s^{\mathrm{x}}_{\mathrm{k,j}} = \frac{\partial\varphi\left(x_{\mathrm{k}}, y_{\mathrm{j}}\right)}{\partial x}$ and $s^{\mathrm{y}}_{\mathrm{k,j}} = \frac{\partial\varphi\left(x_{\mathrm{k}}, y_{\mathrm{j}}\right)}{\partial y}$ are elements in the phase gradient matrix S_{x} and S_{y}. Combining Eqs. (S10)-(S11), the reconstructed phase can be represented in the form of a matrix,

$$\varphi = \begin{bmatrix} \varphi_{1,1} \\ \varphi_{2,1} \\ \cdots \\ \varphi_{K,\mathrm{J}} \end{bmatrix} = (D^{\mathrm{T}}D)^{-1}D^{\mathrm{T}}S, \tag{S12}$$

where φ is the phase matrix to be reconstructed, D is a coefficient matrix, which can be written as,

$$D = \begin{bmatrix} D^{\mathrm{x}} \\ D^{\mathrm{y}} \end{bmatrix} = \begin{bmatrix} -1 & 0 & \ldots & 0 & 1 & 0 & \ldots & \ldots & 0 \\ 0 & -1 & 0 & \ldots & 0 & 1 & 0 & \ldots & 0 \\ \vdots & \vdots & \vdots & \vdots & \vdots & \vdots & \vdots & \vdots & \vdots \\ 0 & \ldots & \ldots & 0 & -1 & 0 & \ldots & 0 & 1 \\ \cdot & \cdot & \cdot & \cdot & \cdot & \cdot & \cdot & \cdot & \cdot \\ -1 & 1 & 0 & \ldots & \ldots & \ldots & \ldots & \ldots & 0 \\ 0 & -1 & 1 & 0 & \ldots & \ldots & \ldots & \ldots & 0 \\ \vdots & \vdots & \vdots & \vdots & \vdots & \vdots & \vdots & \vdots & \vdots \\ 0 & \ldots & \ldots & \ldots & \ldots & \ldots & 0 & -1 & 1 \end{bmatrix}. \tag{S13}$$

S is the phase gradient matrix, which can be written as,

$$S = \begin{bmatrix} S^{x} \\ S^{y} \end{bmatrix} = \frac{L}{24} \begin{vmatrix} 12\left(s^{x}_{1,2} + s^{x}_{1,1}\right) \\ \left(-s^{x}_{1,4} + 13s^{x}_{1,3} + 13s^{x}_{1,2} - s^{x}_{1,1}\right) \\ \left(-s^{x}_{1,5} + 13s^{x}_{1,4} + 13s^{x}_{1,3} - s^{x}_{1,2}\right) \\ \vdots \\ 12\left(s^{x}_{I,J} + s^{x}_{I,J-1}\right) \\ \cdots\cdots\cdots\cdots\cdots\cdots\cdots\cdots\cdots\cdots \\ 12\left(s^{y}_{2,1} + s^{y}_{1,1}\right) \\ \left(-s^{y}_{4,1} + 13s^{y}_{3,1} + 13s^{y}_{2,1} - s^{y}_{1,1}\right) \\ \left(-s^{y}_{5,1} + 13s^{y}_{4,1} + 13s^{y}_{3,1} - s^{y}_{2,1}\right) \\ \vdots \\ 12\left(s^{y}_{K,J} + s^{y}_{K-1,J}\right) \end{vmatrix} . \tag{S14}$$

Text S3. Calibration process of the metalens-assisted single-shot complex amplitude imaging system

Before the actual measurement of the target object, the imaging system needs to be calibrated with a reference plane wave to eliminate additional phase gradients caused by imperfect collimation and additional alignment errors. Here we take the measurement of surface morphology of ultraviolet adhesives in the main text as an example. The background phase gradient terms $\nabla_{x/y}\varphi_{bg}$ can be calculated by the captured shearing interference images (Fig. S2A-B) with a near-collimated incident beam in the absence of the target object. Subsequently, the background phase gradients (Fig. S2C-D) can be calculated from Eq. (S7). The net phase gradient $\nabla_{x/y}\varphi_{net}$ generated by the target object can be written as,

$$\nabla_{x/y}\varphi_{net} = \nabla_{x/y}\varphi_{measured} - \nabla_{x/y}\varphi_{bg}, \tag{S15}$$

where $\nabla_{x/y}\varphi_{measured}$ is the measured phase gradient with the target object inserted. Note that such a calibration process only needs to be performed once after the experimental setup is fixed.

Text S4. Schematic illustration of the geometric relations between Δs and $\Delta s'$, d and d'.

While the splitting distance d' and shearing distance s' of the metalens is designed for plane wave incidence, in an imaging system with a finite object distance d_o, the effective splitting distance d and shearing distance s are different.

The geometric relation between splitting distance d and d' are shown in Fig. S3A and can be written as,

$$\frac{d'}{d} = \frac{f}{d_i}, \tag{S16}$$

where f is the focal length of the metalens, and d_i is the image distance. The imaging formula can be written as,

$$\frac{1}{d_o} + \frac{1}{d_i} = \frac{1}{f}. \tag{S17}$$

Combining Eq. (S16) and Eq. (S17), the effective splitting distance d with a finite d_o can be calculated as,

$$d = (1 + M)d', \tag{S18}$$

where $M = d_i / d_o$ is the magnification ratio.

For the shearing distance, we first consider the imaging process of two dots (green and yellow) on the object plane that are separated by an actual shearing distance of Δs, as shown in Fig. S3B. The distance between the LCP and RCP optical axis is $\Delta s'$. The green dot is fixed on the LCP optical axis. The yellow dot is off-axis imaged to the image plane relative to the RCP optical axis and further interferes with the green dot. The geometric relation between shearing distance Δs and $\Delta s'$ can be calculated as,

$$\Delta s = (1 + 1/M)\Delta s'. \tag{S19}$$

Text S5. Field-of-view of the metalens and the impact of zero-order diffraction.

For the compact complex amplitude imaging system, with collimated light illumination, the field-of-view (FOV) of the imaging system is identical to the aperture size of the metalens, which has a diameter of 2 mm. Due to the finite diffraction efficiency of the metalens, part of the collimated beam is not modulated by the metalens to form the zero-order diffraction.

The geometric relation between the zero-order diffraction region (red) and imaging region (blue) is shown in Fig. S4A. For an object distance d_o = 2.5 cm, the corresponding magnification ratio M = 1.5, and the splitting distance d = 5 mm. The diameter of the imaging area on the image plane is 3 mm, calculated by M·FOV. In this way, while making the most use of the photosensor with a size of 8.5 × 7.1 mm^2, the overlap between the imaging region and zero-order diffraction can also be avoided, as shown in Fig S4B.

For the metalens-based complex amplitude microscopy system, the target object is first imaged by the metalens with a magnification ratio of × 1.75, as shown in Fig. S5. The FOV of the imaging system is designed to be 85 × 85 μm^2, corresponding to the diameter of the imaging region on the image plane at 148 μm, calculated by M·FOV. The splitting distance d' is designed to be 55 μm, corresponding to the effective splitting distance d of 150 μm, calculated by $(1 + M)\,d'$. The effective splitting distance is larger than the diameter of the imaging region, thus avoiding the crosstalk between the x- and y-shearing interference imaging region (two blue areas in the image plane), as shown in Fig. S5.

In addition, the crosstalk between the zero-order diffraction speckle and imaging region was avoided by off-axis imaging in the microscopy system, as schematically shown in Fig. S5. The distance between the target object and the principal optical axis is set to d_a = 100 μm, which is much smaller than the diameter of the metalens. Thus, the center of the imaging region (blue) deviates from the principal optical axis by a distance of 175 μm, calculated by $M \cdot d_a$, away from the zero-order diffraction region (red) to avoid the crosstalk.

After the secondary magnification using a 20× objective lens, the total system magnification ratio is 35. In the polarization camera plane, the diameter of a single shearing imaging region is 3 mm, which also makes full use of the photosensor with a size of 8.5 × 7.1 mm^2. For the current design of the microscopy system, the FOV is still mainly limited by the size of the photosensor.

Text S6. Metalens unit cell design and fabrication

As shown in Fig. S6A, each unit cell of the metalens is composed of a 600-nm-tall single-crystalline silicon nanopillar, which is situated on a sapphire substrate with a thickness of 650 μm. The nanopillar's width W_x and W_y are swept within a range from 100 nm to 250 nm, with the

period P and height H of the nanopillar fixed at 350 nm and 600 nm, respectively. The simulation results for transmittance and phase of the x-polarized incident light are shown in Fig. S6B, C, respectively. Based on this unit cell library, a pair of [W_x, W_y] can be selected for each pair of target transmission phase of x- and y-polarized incident light, as is shown in Fig. S6D, E.

The full phase profile of the metalens that has two pairs of shearing interference PSFs is given by:

$$\phi_{\mathrm{LCP}}(x, y) = \mathrm{angle}\left(\begin{array}{l} \exp\left[ik_0 \left(\sqrt{x^2 + y^2 + f^2} - f \right) + ik_0 \frac{d'}{2f} x + ik_0 \frac{\Delta s'}{2f} y \right] + \\ \exp\left[ik_0 \left(\sqrt{x^2 + y^2 + f^2} - f \right) - ik_0 \frac{d'}{2f} x + ik_0 \frac{\Delta s'}{2f} y \right] \end{array} \right) \tag{S20}$$

$$\phi_{\mathrm{RCP}}(x, y) = \mathrm{angle}\left(\begin{array}{l} \exp\left[ik_0 \left(\sqrt{x^2 + y^2 + f^2} - f \right) + ik_0 \frac{d'}{2f} x - ik_0 \frac{\Delta s'}{2f} y \right] + \\ \exp\left[ik_0 \left(\sqrt{x^2 + y^2 + f^2} - f \right) - ik_0 \frac{d'}{2f} x - ik_0 \frac{\Delta s'}{2f} y \right] \end{array} \right) \tag{S21}$$

where f is the focal length of the metalens, λ = 800 nm is the working wavelength, d' is the splitting distance, $\Delta s'$ is the shearing distance. In order to achieve independent and continuous wavefront modulation for LCP and RCP light, the propagation phase and geometric phase are considered as,

$$\phi_{\mathrm{LCP}}(x, y) = \phi_{\mathrm{prop}}(x, y) + 2\theta(x, y) \tag{S22}$$

$$\phi_{\mathrm{RCP}}(x, y) = \phi_{\mathrm{prop}}(x, y) - 2\theta(x, y) \tag{S23}$$

where θ is the rotation angle of the unit cell, $\phi_{\mathrm{prop}}(x, y) = \phi_x(x, y)$ is the polarized propagation phase. The x- and y-polarized phases and rotation angle of the unit cell can be calculated as,

$$\phi_x(x, y) = \frac{\phi_{\mathrm{LCP}}(x, y) + \phi_{\mathrm{RCP}}(x, y)}{2} \tag{S24}$$

$$\phi_y(x, y) = \frac{\phi_{\mathrm{LCP}}(x, y) + \phi_{\mathrm{RCP}}(x, y)}{2} + \pi \tag{S25}$$

$$\theta(x, y) = \frac{\phi_{\mathrm{LCP}}(x, y) - \phi_{\mathrm{RCP}}(x, y)}{4} \tag{S26}$$

Finally, the geometric parameters of the corresponding unit cell can be selected from the geometric parameter library as shown in Fig. S6D-E. Each meta-atom works as a half-waveplate to allow a high circular polarization conversion efficiency. In Figs. S6B-E, white curves are added to label the selected meta-atoms with a function of half-waveplate. As is shown in Fig. S6B, most of the selected meta-atoms for constructing the metalens hold a near-unity transmittance, which is helpful to allow a relatively high diffraction efficiency of the metalens.

Text S7. Measurement of the PSFs of the metalens

The experimental setup for characterizing the PSFs of the metalens is shown in Fig. S7. We use a supercontinuum laser (SC-PRO-7, YSL) coupled to a monochromator (Omni-λ2007i, Zolix) as the collimated light source (wavelength centered at 800 nm). To avoid the birefringence effect of the metasurface substrate changing the polarization state of the incident light, a linear

polarizer is placed in front of the light source and oriented in the same direction as the crystal axis of the sapphire substrate. The measurement results of PSFs are shown in Fig. 2A in the main text.

Note that if the polarization direction is not aligned with the crystal orientation of the sapphire substrate, the birefringence effect leads to two sheared focal spots with unequal intensity. However, the phase gradients, which are included in the interference term of Eq. 1 of the main text, can still be uniquely calculated by the four-step phase-shifting method. Therefore, the phase reconstruction is not affected by the birefringence effect.

Text S8. Phase measurement for chiral samples

For the measurement of samples with chirality, therefore are two scenarios: samples with circular dichroism and samples with circular birefringence.

For samples with circular dichroism, the polarization-dependent absorbance can result in $I_{LCP} \neq I_{RCP}$, which does not affect the phase reconstruction process.

For samples with circular birefringence, if we assume the sample having a polarization-dependent refractive index of n_{LCP} and n_{RCP}, the reconstructed phase φ_{sum} contain the additional term φ_{chiral}, which can be written as,

$$\varphi_{sum} = \varphi_{OPD} + \varphi_{chiral} = \frac{2\pi}{\lambda}\Delta nL + \frac{2\pi}{\lambda}(n_{LCP} - n_{RCP})L, \quad \text{(S27)}$$

where φ_{OPD} is the optical path difference phase caused by the optical propagation, λ is the wavelength of incident light, Δn is the refractive index difference between the sample and its surrounding environment, and L the free space path length.

In our experiment and most quantitative phase imaging systems, Δn is on the order of 10^{-1}~10^{-2}. On the other hand, circular birefringence in most natural chiral samples, such as biomolecules, is also very weak, with $n_{LCP} - n_{RCP}$ typically on the order of 10^{-4}~10^{-5}. Therefore, for most natural samples, the additional phase difference introduced by chirality is so small such that it can be ignored.

Text S9. Metasurface phase characterization using the metalens-assisted single-shot complex amplitude imaging system

The metalens-assisted imaging system can also be used to characterize the phase distribution of other phase objects, such as a metasurface carrying orbital angular momentum. We design a metasurface consisting of cylindrical crystalline silicon nanopillars on a sapphire substrate (Fig. S8A), carrying a spiral phase distribution of 2π. The nanopillar's diameter D is swept within a range of 100 nm to 203 nm, when the period P and height H of the nanopillar remain fixed at 420 nm and 600 nm, respectively. The simulated transmittance and phase of the metasurface as a function of the nanopillar's diameter D the metasurface for a normally incident plane wave are shown in Fig. S8B. The optical microscope image and scanning electron microscope image of the fabricated metasurface are shown in Fig. S8C-D, respectively. The captured polarized shearing images are shown in Fig. S8E. The calculated phase gradients and reconstructed complex amplitude profile of the metasurface are shown in Fig. S8F-G, showing close agreement with the designed phase profile.

The measured phase distribution of the orbital angular momentum (OAM) metasurface exhibits a spiral phase distribution with a maximum phase difference of close to 2π, but the phase distribution near the singularity deviates from the theoretical value.

The phase reconstruction error near the singularity is mainly due to two issues. The first one is the limited spatial sampling interval. For the stand-alone metalens used to characterize the OAM metasurface, it has a relatively large shearing distance Δs = 25 μm and a relatively low numerical aperture (NA) of 0.066. Therefore, the phase image near the phase singularity is blurred. The second issue is that the measurable phase gradient is limited according to Eq. (2) of the main text, since the value range of the arc tangent function is limited to 0 to 2π. When the phase gradient of the sample exceeds $2\pi/\Delta s$, the phase wrapping problem may produce unexpected additional phase gradient errors. To address these issues, one may design an imaging system with a smaller shearing distance and larger NA, or develop more advanced phase unwrapping algorithms.

Text S10. Measurement of the phase resolution targets with different thicknesses

The 1951 USAF phase resolution target (Quantitative Phase Microscopy Target, Benchmark Technologies) has seven sets of phase objects of different thicknesses, measured by the white light interferometer as 361 nm, 300 nm, 253 nm, 194 nm, 153 nm, 103 nm, and 57 nm, respectively, which are used as the ground truth. Combined with the four polarization shearing interference patterns of the resolution target (Group 6, Element 1) captured by our system, the phase gradients and target thickness can be reconstructed. Such a process was repeated for seven phase resolution targets with different thicknesses. The results of Sample No.1 (361 nm), measured by our system, have been shown in Fig. 4C-D of the main text. The measurement results of the other six phase samples are shown in Fig. S9A-F. The measured averaged thickness closely matches the results obtained by the WLI, as shown in Fig. 4E in the main text.

For the spatial resolution of the complex amplitude imaging system, there are two main limiting factors, including 1) the diffraction limit of the imaging system, and 2) the spatial sampling interval. For instance, in the complex amplitude microscopy system, the diffraction limit of the imaging system is 1.31 μm, as calculated from the numerical aperture of the metalens. The spatial sampling interval is the shearing distance of 1.57 μm.

For the phase resolution $\delta\varphi$ of the imaging system, it may be calculated as,

$$\delta\varphi = \delta s \cdot \nabla_{x/y}\varphi_{min}, \tag{S28}$$

where δs is the spatial resolution, and $\nabla_{x/y}\varphi_{min}$ is the smallest measurable phase gradient. We found it difficult to identify an analytical solution of $\nabla_{x/y}\varphi_{min}$, since it is affected by many factors, including the dynamic range of the polarization camera and the source noise. Experimentally, the verified smallest detectable phase gradient is 42 mrad/μm, calculated from the average phase gradient in the black box in Fig. S9F. Note that this verified smallest detectable phase gradient is limited by the available phase target with a finite thickness. The actual smallest detectable phase gradient of the system may have a smaller value.

Text S11. Measurement of relative phase accuracy, spatial and temporal noise levels

The random intensity fluctuation of the light source and the noise of the polarization

camera can lead to the spatial and temporal noise of the measured phase gradient. To quantify the spatial noise level, we measured the phase distribution of a plane wave using the metalens-based complex amplitude microscopy system. The measurement area is 60 × 60 μm^2 and consists of 287 × 287 sampling points. The phase gradients of an ideal plane wave should be zero. The measured *x*- and *y*-phase gradient errors caused by spatial noise are shown in Fig. S10A.

Combined with the captured *x*- and *y*-phase gradients, the reconstructed phase distribution of the plane wave is shown in Fig. S10B. The relative phase accuracy is defined as the root-mean-square error of the reconstructed plane reference wave (49). For a comprehensive assessment of the relative phase accuracy, we continuously captured 50 frames of the phase distribution of the plane wave at a time interval of 5 s. The corresponding average mean root-mean-square of 50 frames is 0.0021λ, with the working wavelength λ = 800 nm.

The histograms of *x*- and *y*-phase gradient errors are shown in Fig. S10C-D. The error histogram conforms to a Gaussian distribution and can be described as,

$$f(\nabla\varphi) = ae^{-\frac{\nabla\varphi^2}{2\sigma^2}}, \tag{S29}$$

where $\nabla\varphi$ is the phase gradient error that needs to be fitted, a is the peak of the Gaussian function and σ is the standard deviation of the Gaussian function and also determines the noise level. By Gaussian fitting analysis, the spatial noise level of the phase gradient along *x*- and *y*- direction are 26.08 mrad/μm and 25.78 mrad/μm, respectively, which are defined as twice the standard deviation σ. The average phase gradient spatial noise level along both in-plane directions is 25.93 mrad/μm.

For the measurement of temporal noise levels, we selected the green and black circle areas in Fig. S10E, which contributed most to the phase reconstruction. The fluctuation of *x*- and *y*-phase gradients over time for the seven phase resolution targets in Group 6 Element 1 of different thicknesses are shown in Fig. S10F-G. The temporal noise level is calculated by $\sqrt{\frac{1}{N}\sum_{i=1}^{N}(\overline{\nabla\varphi} - \nabla\varphi_i)^2}$, where $N = 60$ is the number of acquisitions, $\nabla\varphi_i$ is the captured phase gradient at the *i*-th time and $\overline{\nabla\varphi}$ is the average phase gradient over the measurement time. The average time noise level of different *x*- and *y*-phase gradients is 2.88 mrad/μm.

Text S12. Measurement of the spatial resolution of the metalens-based complex amplitude microscopy system

The spatial resolution of the complex amplitude imaging system includes phase spatial resolution and imaging spatial resolution, which can be measured by a 1951 USAF phase and intensity resolution target, respectively.

The spatial resolution of the phase image depends on the shearing distance Δs and the diffraction limit of the imaging system. As shown in Fig. 11A, the captured *x*- and *y*-phase gradients of the 300-nm-thick Group 7, Element 3 and 4 of 1951 USAF phase resolution target overlap with each other due to diffraction effects, resulting in a blurred light intensity image (Fig.11B) and thickness reconstruction result (Fig.11C).

For the different groups and elements of the 1951 USAF resolution target, the linewidth is calculated as,

$$\text{Linewidth} = 10^3 / 2^{\text{Group} + (\text{Element}-1) / 6 + 1} \ (\mu\text{m}). \quad \text{(S30)}$$

The linewidths of Group 7, Elements 3 and 4 of the 1951 USAF intensity resolution targets are 3.10 μm and 2.76 μm, respectively, corresponding to the imaging spatial resolution of 6.20 μm and 5.52 μm, respectively. To further improve the spatial resolution of the imaging system, one could design a metalens with a higher NA. In addition, one could further optimize the phase distribution of the metalens to correct off-axis aberrations and better match it with a standard microscope system.

To evaluate the system's spatial resolution for intensity imaging, we use the 1951 USAF intensity resolution target as the target object. The imaging spatial resolution of the metalens-based complex amplitude microscopy system is mainly limited by the sheared PSFs. On the image plane, two replicated LCP and RCP images are spatially shifted by a distance of Δs along x- or y-direction, overlapping with each other, resulting in reduced spatial resolution, as shown in Fig. S12A, B. The linewidths of Group 7, Elements 5 and 6 of the 1951 USAF intensity resolution target are 2.46 μm and 2.19 μm, respectively, corresponding to the imaging spatial resolution of 4.92 μm and 4.38 μm, respectively.

Supplementary Figure

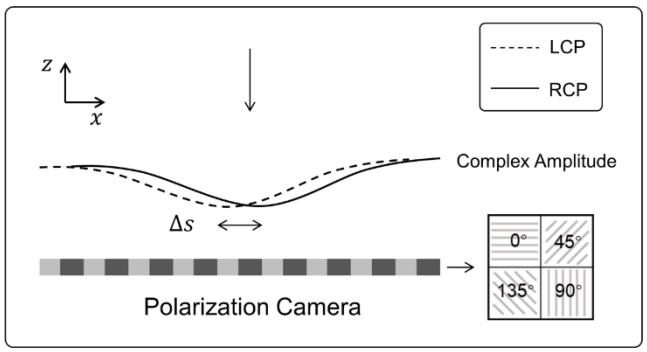

Fig. S1. Schematic diagram of the shearing interferometry based on polarization phase shift. Two replicated left- and right-handed circularly polarized (LCP and RCP) light field are separated a shearing distance Δs in the *x*- direction and interfere on the polarization camera.

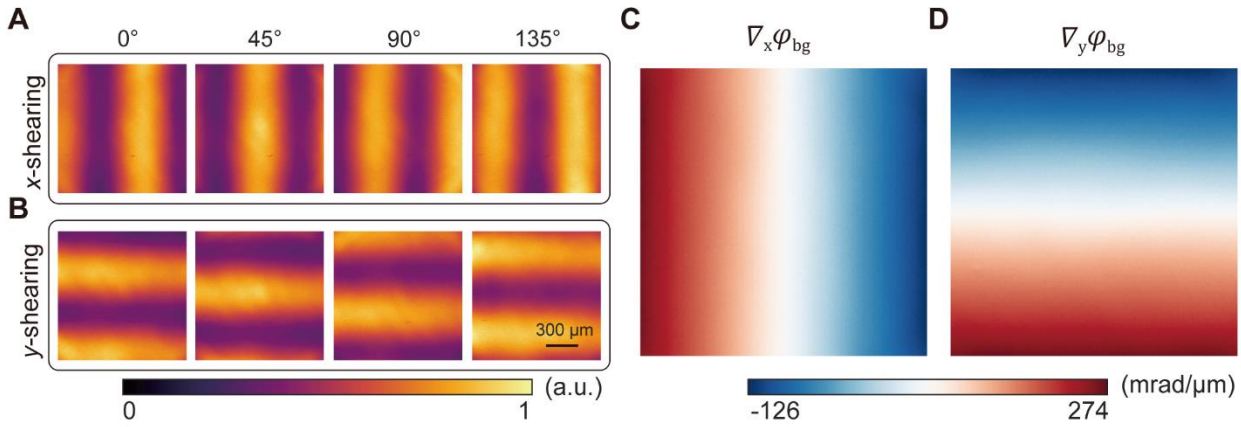

Fig. S2. Calibration process of the metalens-assisted single-shot complex amplitude imaging system. (**A**-**B**) Captured *x*- (**A**) and *y*- (**B**) shearing light intensity images of 0°, 45°, 90°, and 135° linear polarization state, respectively without phase object using the minimalist complex amplitude imaging system. (**C**-**D**) Calculated background phase gradient along the *x*-direction (**C**) and *y*-direction (**D**), respectively.

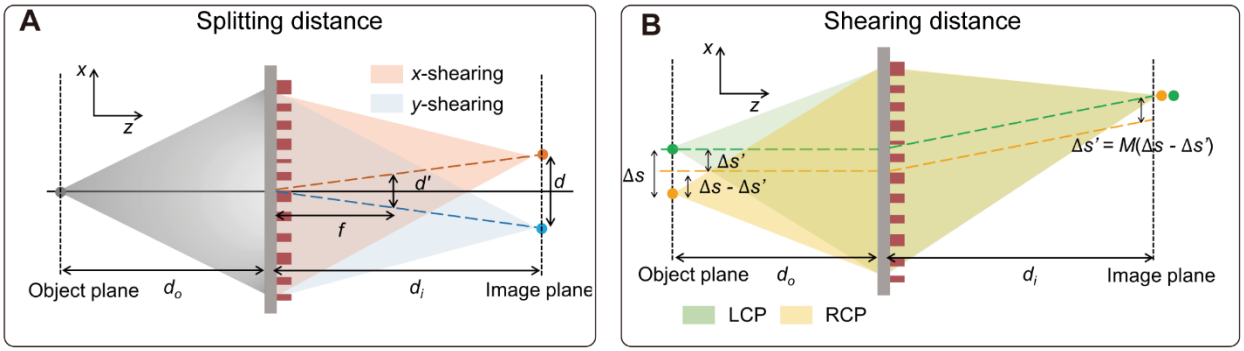

Fig. S3. Schematic illustration of the geometric relations of the splitting distance and shearing distance. (**A**) Schematic diagram of the geometric relation between *d* and *d'*. The gray dot at the object plane is imaged by the metalens as two dots (orange and blue) in the image plane, separated by a distance *d* along the *x*-direction. Each imaged dot contains a pair of shearing interference PSFs. (**B**) Schematic diagram of the geometric relation between Δ*s* and Δ*s'* for *x*-shearing interference. The green and yellow dashed lines denote the optical axis for LCP and RCP incident light, respectively. The green and yellow dots with a distance of Δ*s* at the object plane are imaged and interfered at the image plane. *M* is the magnification ratio of the imaging system.

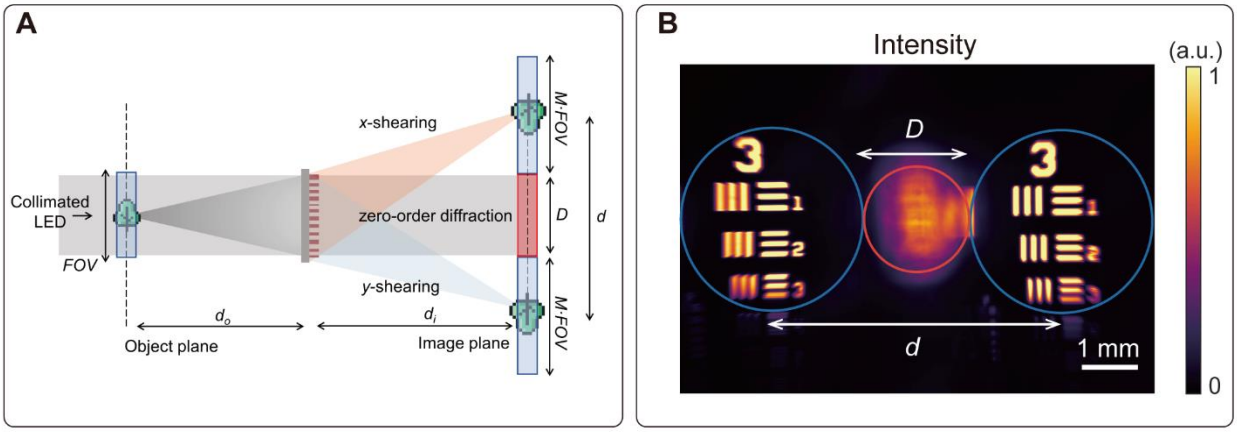

Fig. S4. Field-of-view of the metalens and the impact of zero-order diffraction in the compact complex amplitude system. (**A**) Schematic diagram of the field-of-view and the zero-order diffraction in the compact complex amplitude imaging system, where d_o is the object distance, d_i is the imaging distance, M is the magnification ratio of the imaging system, and D is the diameter of the metalens. The red and blue regions are the zero-order diffraction region and the imaging region, respectively. (**B**) Captured intensity image using the compact complex amplitude imaging system.

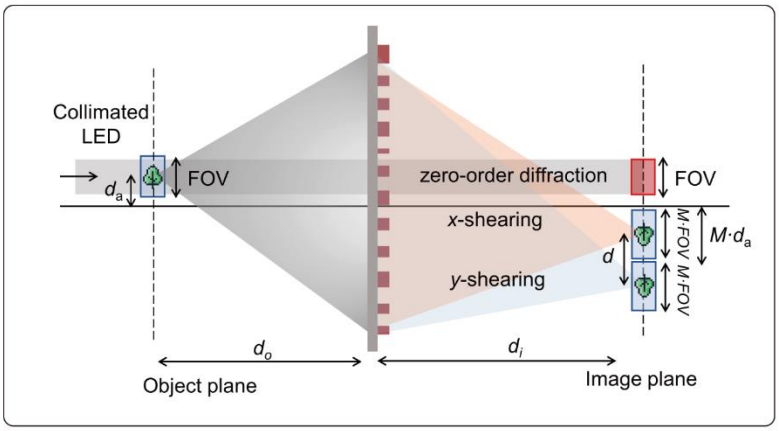

Fig. S5. Schematic diagram of the field-of-view and the zero-order diffraction in the metalens-based complex amplitude microscopy system. The d_o is the object distance, d_i is the imaging distance and M is the magnification ratio of the metalens. The black dashed line denotes the principal optical axis. The red and blue regions denote the zero-order diffraction region and the imaging region, respectively.

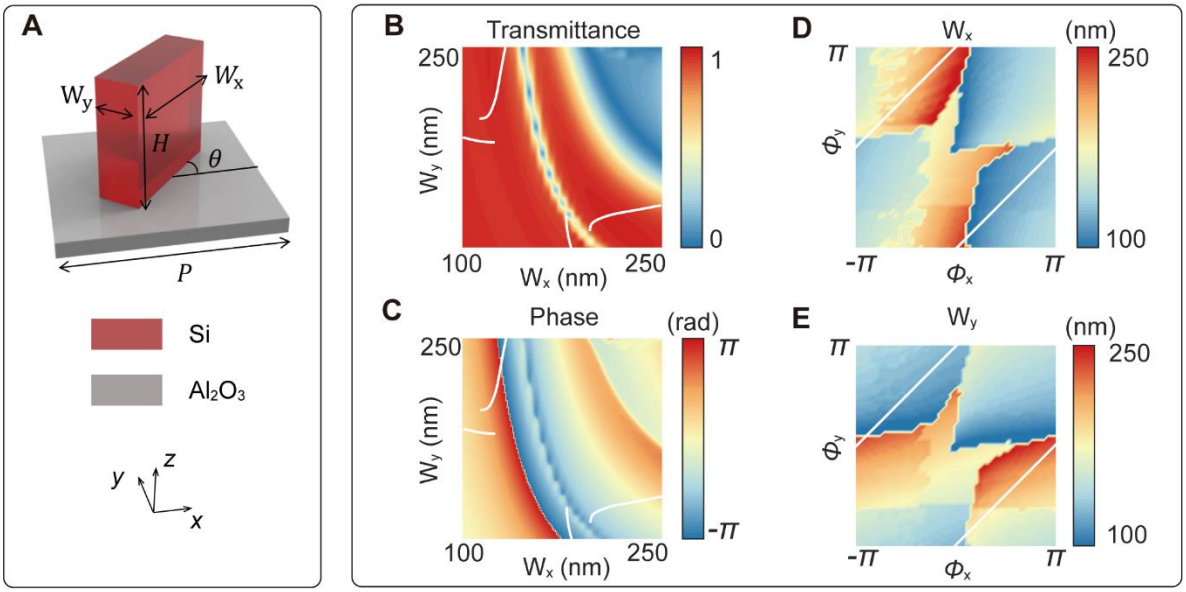

Fig. S6. Metalens unit cell design. (**A**) Tilted view of the unit cell of the metalens. (**B**) Simulated transmittance for *x*-polarized normally incident plane wave when the rotation angle θ = 0°. (**C**) Simulated transmission phase for x-polarized normally incident plane wave when the rotation angle θ = 0°. (**D-E**) Selected width W_x and W_y of the nanopillars for independent and continuous control of the transmission phase of *x*- and *y*-polarized incident light. In panel B-E, white curves are used to label the selected meta-atoms with a function of half waveplate.

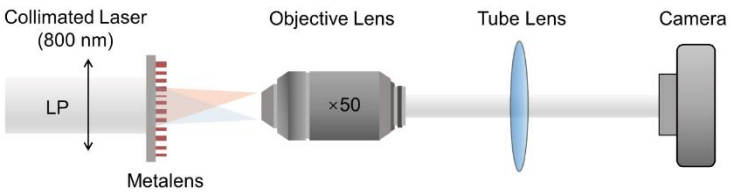

Fig. S7. Schematic of the experimental setup for the measurement of the metalens' PSFs. The linear polarizer (LP) is oriented in the same direction as the crystal axis of the sapphire substrate.

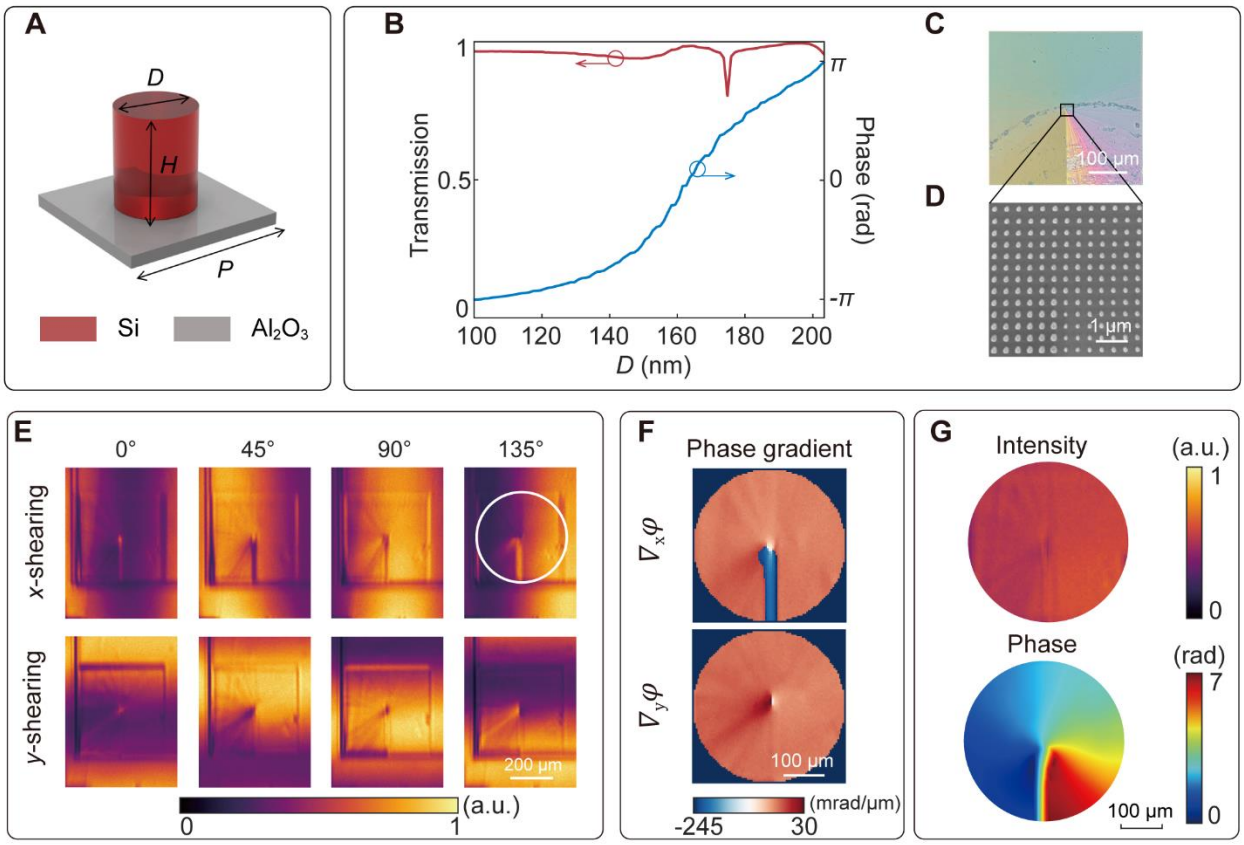

Fig. S8. Metasurface phase characterization using the metalens-assisted single-shot complex amplitude imaging system. (**A**) Tilted view of the unit cell of a metasurface carrying orbital angular momentum. (**B**) Simulated transmittance and phase of the metasurface as a function of the nanopillar's diameter *D* for a normally incident plane wave. (**C-D**) Optical microscopy image (**C**) and scanning electron microscopy image (**D**) of the fabricated metasurface. (**E**) Captured *x*- and *y*-shearing light intensity images at 0°, 45°, 90°, and 135° linear polarization channel, respectively. (**F**) Calculated phase gradients along the *x*- and *y*-direction, respectively. The reconstruction region is marked as the white-circled area in (**E**). (**G**) Reconstructed complex amplitude profile of the metasurface.

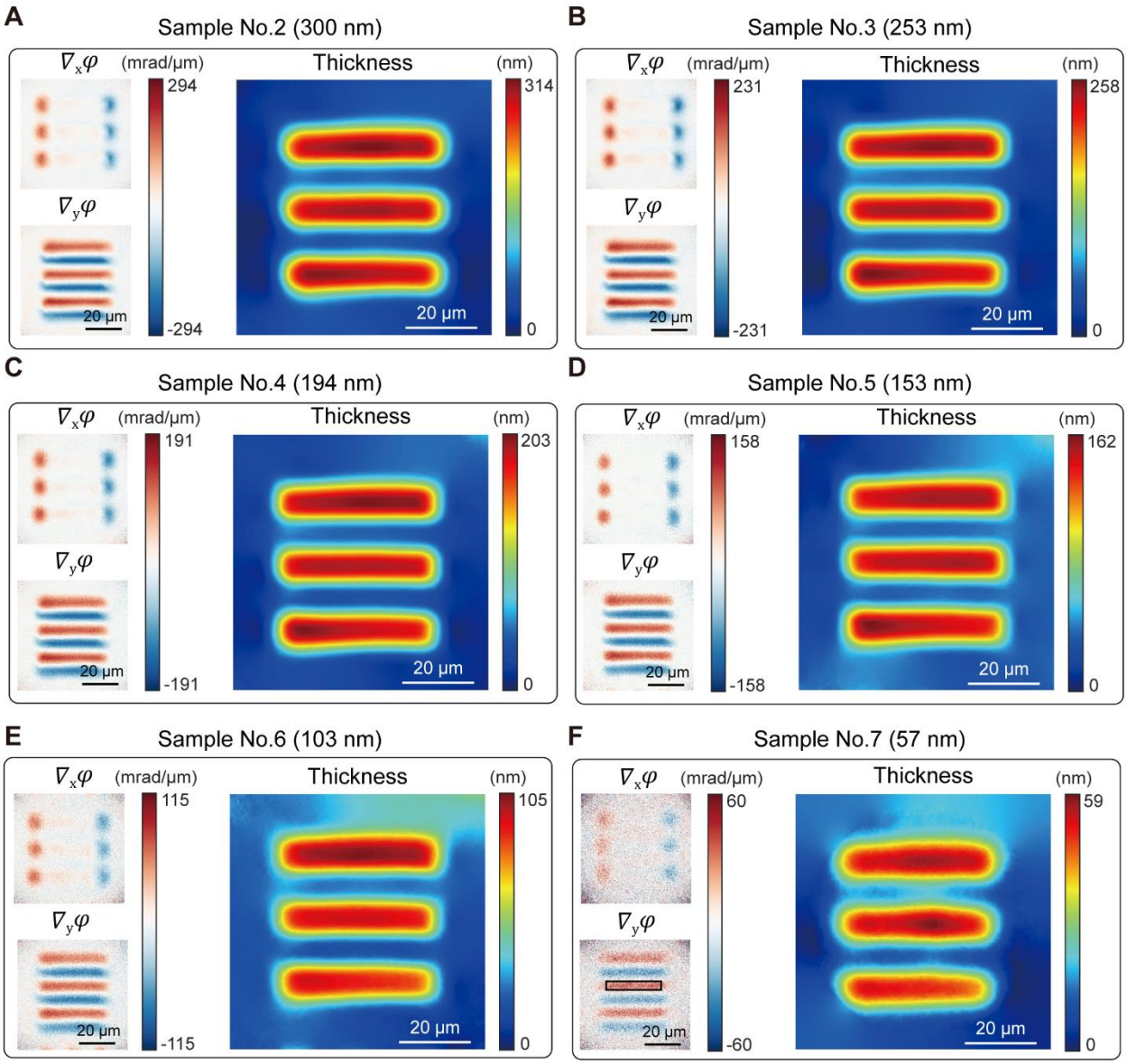

Fig. S9. Measurement of the phase resolution targets with different thicknesses. (A-F) Measured phase gradients and thickness of phase resolution targets with different thicknesses using the metalens-assisted complex amplitude microscopy system. The thicknesses measured by the white light interferometer are 361 nm, 300 nm (**A**), 253 nm (**B**), 194 nm (**C**), 153 nm (**D**), 103 nm (**E**), and 57 nm (**F**) for Sample No.1-7, respectively. The measurement results for Sample No.1 (361 nm) are shown in Fig. 4C-D of the main text.

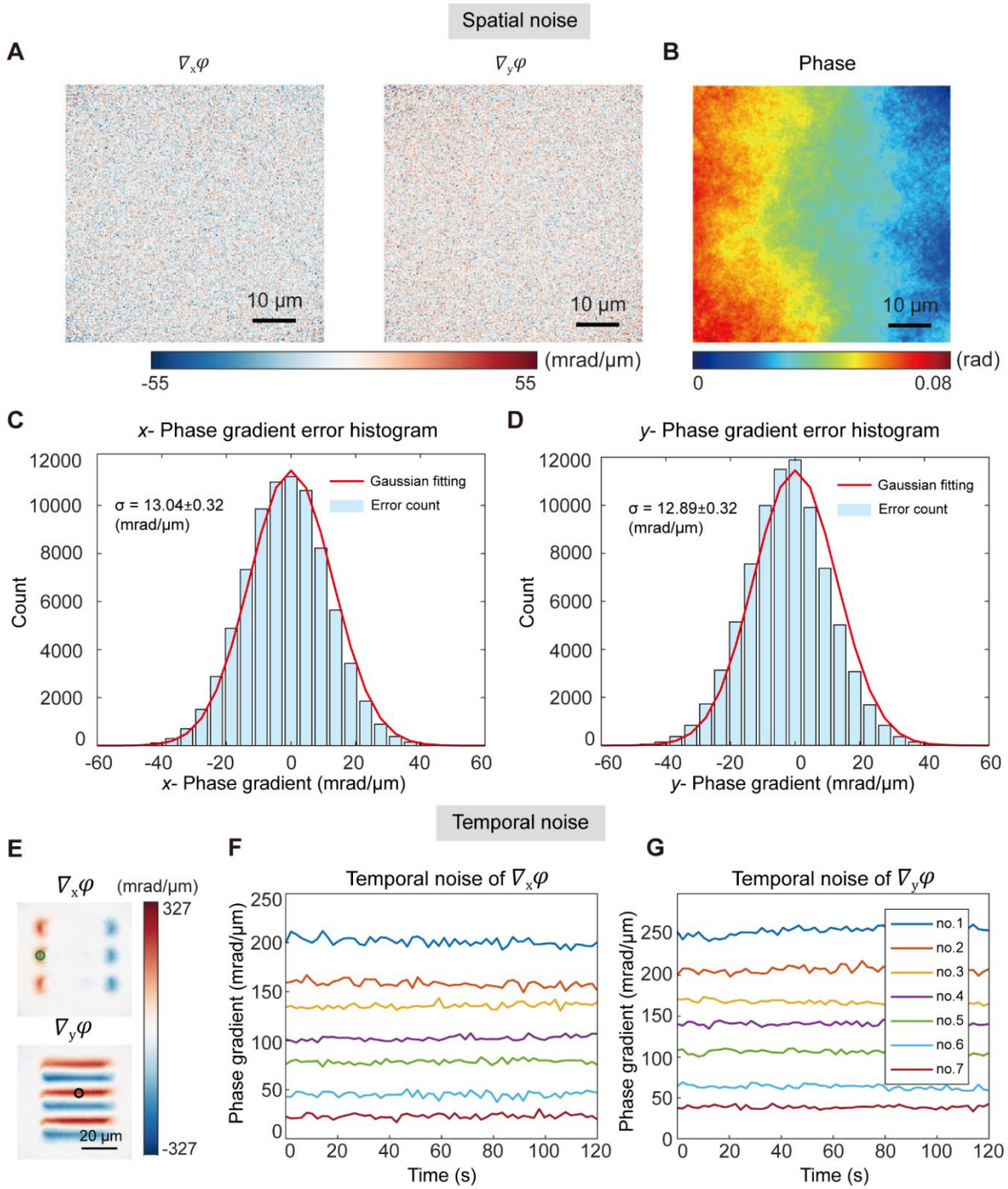

Fig. S10. Measurement of relative phase accuracy, spatial and temporal noise levels for the metalens-assisted complex amplitude microscopy system. (**A**) Captured phase gradients along the *x*- and *y*-direction when the collimated light incident within a detection area of 60 × 60 μm^2. (**B**) Reconstructed phase distribution based on phase gradients along the *x*- and *y*-direction, respectively. (**C**-**D**) Histograms of the captured phase gradient along the *x*- and *y*-direction, respectively. (**E**) Captured *x*- and *y*-phase gradients of the 361-nm thick phase resolution target in Group 6 Element 1 at t = 0 s. (**F**-**G**) Measured time-dependent *x*- and *y*-phase gradients at the green and black circle area in (**E**). The acquisition time interval is 2 s.

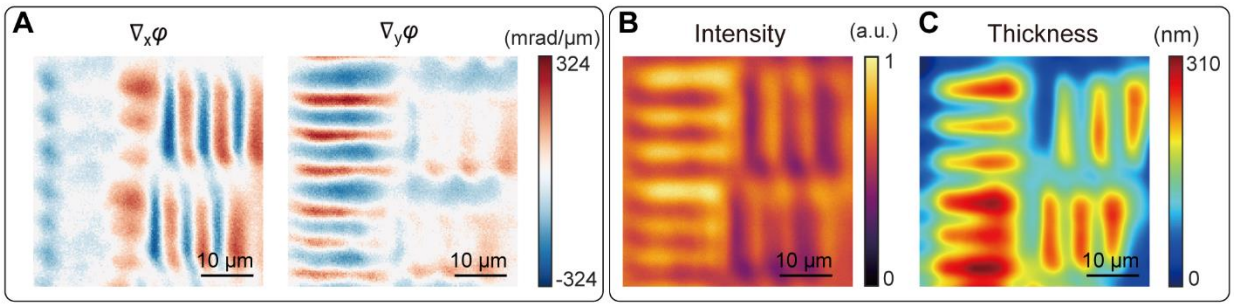

Fig. S11. Measurement of the phase spatial resolution of the metalens-based complex amplitude microscopy system. (**A**) Captured *x*- and *y*- phase gradient of the 300-nm thick Group 7 Element 3, 4 of 1951 USAF phase resolution target using the metalens-based complex amplitude microscopy. Each element consists of three bars with a certain linewidth. (**B**) Captured intensity image of the phase resolution target. (**C**) Reconstructed thickness of the phase resolution target.

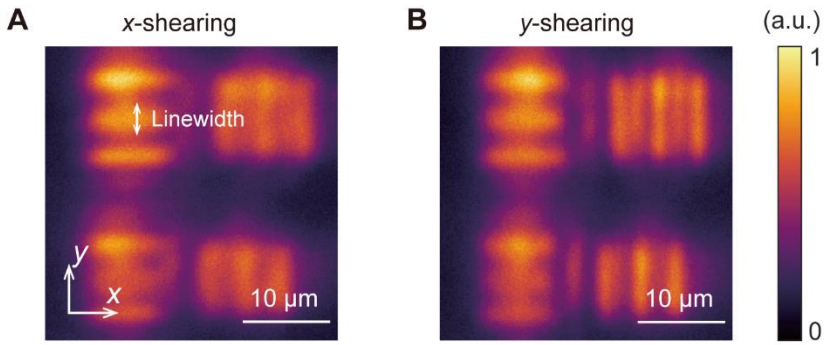

Fig. S12. Measurement of the intensity spatial resolution of the metalens-based complex amplitude microscopy system. (**A-B**), Captured *x*-(**A**) and *y*-(**B**) shearing images of the Group 7, Element 5 and 6 of 1951 USAF intensity resolution target using the metalens-based complex amplitude microscopy. Each element consists of three bars with a certain linewidth.

Supplementary Movies

Movie S1. Label-free observation of the moving paramecium using the metalens-based complex amplitude microscopy system at a frame rate of 10 Hz.

Movie S2. Dynamic surface metrology of the uncured UV adhesive sample using the metalens-assisted single-shot complex amplitude imaging system at a frame rate of 50 Hz.